Chen *et al.*
BMC Complementary Medicine and Therapies (2025) 25:217
https://doi.org/10.1186/s12906-025-04957-0

BMC Complementary Medicine and Therapies

RESEARCH Open Access

PLGA-based herb Toosendanin delivery system for efficient therapy of oral squamous cell carcinoma

Lingling Chen[1†], Cheng Feng[1†], Zhenyu Shi[1], Jianzhe Wang[1], Tao Wang[1], Yibing Wang[1], Lisong Lin[2*] and Ye Wu[1*]

Abstract

Oral squamous cell carcinoma (OSCC) is a significant public health issue worldwide. Conventional chemotherapeutic agents do not adequately meet the treatment demands because of their low efficacy and adverse side effects. Toosendanin (TSN) is a natural extract with potential anticarcinogenic activity. Nonetheless, its clinical application is constrained by its poor water-solubility and limited bioavailability. Therefore, we prepared TSN-loaded poly (lactic-co-glycolic acid) nanoparticles (TSN-PLGA NPs) to improve the water-solubility of TSN and potentially further enhance its bioavailability. TSN-PLGA NPs were synthesized and characterized, and we showed their exceptional properties for sustained release in vitro. TSN-PLGA NPs exhibited cytotoxic effects against OSCC cells, potentially inhibiting proliferation and promoting apoptosis by inducing cell-cycle arrest in the S-phase at low concentrations. RNA-sequencing analysis revealed the potential regulation of OSCC cell viability by TSN-PLGA NPs through signaling pathways such as JAK/STAT and PI3K–Akt. Furthermore, animal models provided evidence of the in vivo antitumor activity of TSN-PLGA NPs, with no observable side effects in nude mice, which indicated potential biocompatibility. Consequently, TSN-PLGA NPs may be a promising chemotherapy candidate for OSCC treatment.

Keywords Toosendanin, Oral squamous cell carcinoma, PLGA, Nanomedicine, EPR effect

Introduction

Oral carcinoma is a prevalent malignant tumor of the head and neck area, and ranks 16 th in terms of incidence among all cancers. Oral squamous cell carcinoma (OSCC) is a predominant pathological subtype, and comprises 90% of cases [1, 2]. According to the estimation provided by National Cancer Institute (NCI), lip and oral cavity cancer accounts for approximately 54,540 new cases and 11,580 deaths in the United States in 2023 [3]. Moreover, due to the anatomical and physiological characteristics of the oral and maxillofacial region, which is rich in lymphatic tissue and blood supply and undergoes frequent muscle movements, OSCC is prone to early lymph node metastasis and late distant metastasis, thereby greatly compromising the prognosis and reducing survival of patients [4]. The 5-year overall survival rate in OSCC patients is generally below 60%, which indicates an unfavorable prognosis and presents a substantial obstacle for the management of the disease [5]. Currently, the primary treatment approach for localized OSCC entails the surgical removal of the primary tumor and

†Lingling Chen and Cheng Feng contributed equally to this work.

*Correspondence:
Lisong Lin
dr_lls@fjmu.edu.cn
Ye Wu
wuye@fjmu.edu.cn
[1] Fujian Key Laboratory of Oral Diseases & Stomatological Key Lab of Fujian College and University, School and Hospital of Stomatology, Fujian Medical University, Fuzhou 350002, Fujian Province, China
[2] Department of Oral and Maxillofacial Surgery, The First Affiliated Hospital of Fujian Medical University, Fuzhou 350004, Fujian Province, China

affected lymph nodes. Adjuvant radiotherapy or chemotherapy may follow, depending on the disease stage [6]. Nevertheless, the therapeutic efficacy of conventional chemotherapy drugs is limited, and they are associated with notable adverse effects, including bone marrow suppression, impairment of liver and kidney function, and neurotoxicity [7]. The current preventive and treatment strategies for oral cancer are inadequate in addressing the public health demands. Consequently, it is important to explore innovative and effective methods for managing OSCC.

Natural herbs–derived substances, including bioactive elements, raw extracts, and pure compounds, have been attracting growing attention of researchers in the context of their potential contribution to cancer treatment. Extensive research and data indicate that over 50% of approved anticancer drugs are derived from natural compounds or herbal derivatives. As an effective anticancer drug extracted from plant-derived natural products, paclitaxel has been proven capable of interfering with the signaling pathways of various cancers and inhibiting the proliferation of cancer cells, and widely used in clinical treatment [8]. Inspired by this, a growing number of compounds derived from herbs or traditional Chinese medicine are being applied in clinical studies for cancer treatment. Toosendanin (TSN), which is extracted from toosendan tree, is a compound that consists of tetracyclic triterpenoids. Nowadays, with deep research, its significant value in scientific research, clinical medicine, and agriculture has been found [9]. Previous studies have substantiated its efficacy in alleviating pain, mitigating inflammation, countering botulinum toxin, and combating bacterial infections [10, 11]. TSN also possesses antiproliferative and apoptosis-inducing properties in vitro against several human cancer cells, including gastric cancer, colorectal cancer, liver cancer, and breast cancer [12–16]. However, the poor water solubility, low bioavailability, and undesirable side effects have limited the clinical application of TSN. Although TSN exhibits a fast oral absorption rate and clearance in mouse plasma, its absolute bioavailability is reported to be only 9.9% [17]. Previous studies of TSN side effects have indicated that the hepatic damage observed in mice as a result of TSN exposure may be associated with a reduced level of glutathione, as well as compromised mitochondrial function and abnormal lipid metabolism [18]. Considering the potent anticancer activity of TSN, structural modifications of TSN and the design of targeted drug delivery systems to improve its water-solubility and bioavailability hold significant clinical value.

Compared with conventional pharmaceuticals, nanomedicines offer several advantages such as enhanced drug solubility, passive tumor targeting and accumulation, controlled drug release, and reduced systemic side effects [19, 20]. In recent years, a variety of biodegradable polymers, both natural and synthetic, have been employed biomedical applications, especially in drug delivery and release systems [21, 22]. Interestingly, poly (lactic-co-glycolic acid) (PLGA) is a biodegradable polymer material with good biocompatibility and biodegradability and has widely been used in drug delivery systems [23]. In contrast to inorganic nano-delivery systems, which might be often associated with systemic toxicity and instability, PLGA can degrade into lactic acid and glycolic acid, which are ultimately cleared as water and carbon dioxide. Furthermore, by encapsulating chemotherapy drugs in PLGA, the drugs can be slowly released into tumor tissues while avoiding rapid degradation in the blood or filtration by the kidneys, which improves drug efficacy and reduces side effects. In addition, PLGA nanoparticles possess good stability and prolonged circulation time in blood vessels, which can extend the circulation time of drugs in the body and facilitate their accumulation at the tumor site, thereby enhancing the antitumor effect of the medications. Overall, PLGA-encapsulated chemotherapy is a promising treatment approach because it can improve drug targeting and efficacy while reducing side effects [24].

In summary, TSN may be a promising anticancer drug candidate, but its therapeutic efficiency in OSCC requires further investigation. Herein, we prepared TSN-loaded PLGA nanoparticles (TSN-PLGA NPs) and verified the antitumor activity of TSN and TSN-PLGA NPs through in vitro studies. Previous animal model studies have indicated that TSN may mediate lysosomal dysfunction, thereby causing acute liver injury in mice and zebrafish [25–27]. Consequently, we constructed a cell line–derived xenograft (CDX) model to investigate the efficacy of the drug after in vivo metabolism, while also assessing the in vivo safety of TSN-PLGA NPs. The tumor microenvironment (TME) plays a pivotal role in the growth and migration of tumors [28]. In comparison to the CDX model, a patient-derived xenograft (PDX) model will be able to retain the original structure and molecular characteristics of the primary tumor, accurately replicating the in vivo TME [29]. Therefore, we extended our research from the CDX model to further establish PDX model for in vivo studies. We anticipate that the PDX model will improve the precision of predicting drug efficacy and its anti-tumor effects by more accurately simulating in vivo tumor microenvironment processes.

Materials and methods

Materials

TSN and 5-fluorouracil (5-FU) were purchased from Med Chem Express (Shanghai, China). PLGA (MW

38–54 kDa), dimethyl sulfoxide (DMSO), and polyvinyl alcohol (PVA, MW 145 kDa) were purchased from Sigma Aldrich (St. Louis, MO, USA). Methanol (MeOH), ethyl alcohol, water (HPLC grade), acetonitrile, and dichloromethane (DCM) were purchased from Xilong Scientific (Guangzhou, China). A dialysis membrane (MWCO = 3.5 kDa) was purchased from Spectrum Laboratories Inc. (Rancho Dominguez, CA, USA), and a cryoprotectant D-trehalose was purchased from BioFroxx (Einhausen, Germany). Double-distilled water (ddH_2O) was used for all experiments.

Acquisition of tissue samples

Fresh tumor tissues of oral OSCC were obtained from the First Affiliated Hospital of Fujian Medical University. The patients signed a written informed consent. The study was approved by the Ethics Committee of the Fujian Medical University.

Cell culture and mice

Normal human oral epithelial cells (HOEC) and OSCC cell lines (CAL27 and HN6) were obtained from the Fujian Key Laboratory of Oral Diseases. The cells were cultured in dulbecco's modified eagle medium (DMEM, Gibco, Shanghai, China) with 10% fetal bovine serum (FBS, SORFA, Beijing, China), and kept in humidified incubators with 5% CO_2 at 37 °C.

BALB/C-nude mice were provided by SLAC Laboratory Animal Co., Ltd. (Shanghai, China). The animal experimental protocols were approved by the Ethics Committee of Fujian Medical University.

Preparation of TSN-PLGA NPs

The TSN-PLGA NPs were prepared by using a double emulsion-solvent evaporation method [30]. Briefly, TSN (10 mg) was dissolved in 700 μL of ethanol. Then, 800 μL of ddH_2O was added. PLGA (300 mg) was dissolved in 25 mL of DCM. Then, the TSN solution was added dropwise into the PLGA solution, and the mixture was dispersed for another 20 min using an ultrasonic oscillator to form a W/O primary emulsion. PVA (53 mg) was dissolved in 100 mL of ddH_2O and stirred using a magnetic stirrer at 800 rpm for 4 h to form a PVA solution (W2). The entire W/O primary emulsion was transferred to a conical flask, and W2 was added dropwise while being stirred with a mechanical stirrer at 1,800 rpm for 20 min. Then, the solution was treated with an ultrasonic processor (20,000 Hz, 4 °C) for 15 min and stirred at room temperature to remove the residual DCM. The supernatant was discarded by centrifugation (4 °C, 12,000 rpm, 45 min), and the precipitate was reconstituted in 20 mL of ddH_2O. The cryoprotectant D-trehalose was added. Finally, the NPs were obtained after freeze-drying (Fevik TS8606, Shanghai, China).

Characterization of TSN-PLGA NPs

The structure of TSN-PLGA NPs was examined by scanning electron microscopy (SEM, Frequency Electronics Quanta450, OR, USA) and transmission electron microscopy (TEM, Frequency Electronics Tecnai G2, OR, USA). TSN-PLGA NPs solution (containing TSN at a concentration of 200ug/ml) was prepared using ddH_2O. After gold coating under vacuum conditions, the samples were observed under SEM. In addition, after staining with phosphotungstic acid, TSN-PLGA NPs were observed using TEM.

The dynamic light scattering (DLS) method was employed to measure the particle size distribution and polydispersity index (PDI) of TSN-PLGA NPs, utilizing an Anton Paar Sur-PASS 3 instrument (Anton Paar, Austria). Additionally, the zeta potential (ZP) of TSN-PLGA NPs was determined using the same instrument.

The drug loading (DL) and encapsulation efficiency (EE) of TSN in TSN-PLGA NPs were determined using high-performance liquid chromatography (HPLC). The chromatographic column used was Agilent ZORBAX Eclipse XDB-C18 (250 mm × 4.6 mm, 5 μm). The mobile phase consisted of 0.1% formic acid and acetonitrile (40:60, v/v). The flow rate was set at 1.0 mL/min. The UV detection wavelength was 210 nm. The measurement volume was 10 μL. The following equations were used to calculate DL and EE:

$$\mathrm{DL}(\%) = \left(\frac{\text{Quantity of Loaded drug in Nanoparticles}}{\text{Quantity of Nanoparticles}}\right) \times 100\% \quad (1)$$

$$\mathrm{EE}(\%) = \left(\frac{\text{Quantity of Loaded drug in Nanoparticles}}{\text{Initial Quantityof Drug Added}}\right) \times 100\% \quad (2)$$

Protein adsorption assay

To investigate protein adsorption by prodrug-based nanoparticles, bovine serum albumin (BSA) was chosen as the model protein. Free TSN (150ug/ml), nanoparticles (containing TSN at a concentration of 150 μg/mL) were co-incubated with BSA (120 μg/mL) in PBS (pH 7.4) at 37 °C. At various time points, 200 μL aliquots of each sample were centrifuged (14,000 g, 15 min) to facilitate the precipitation of adsorbed protein aggregates. The BSA standard curve was then established using a BCA protein assay kit (Beyotime Biotechnology Shanghai, China) following the manufacturer's instructions. The concentration of unadsorbed protein was measured using a microplate reader (Thermo Scientific, USA) under the

same conditions. The proportion of adsorbed protein was subsequently calculated at each time point.

In vitro *release study*

The drug release curves of TSN-PLGA NPs in vitro over a period of 36 h were assessed using the dialysis bag method [31]. In total, 150 mg of TSN-PLGA NPs was dissolved in PBS buffer (pH 5.4 or 7.4, 1.5 mL). The solution was quickly transferred into a prepared dialysis bag (MWCO 3.5 kDa), immersed in PBS buffer (pH 5.4 or 7.4, 2 mL) solution, and placed in a 37 °C water bath shaker. At specific time points (0.5, 1, 2, 3, 4, 6, 8, 12, 24, and 36 h), 200 μL was removed from the surrounding solution and replaced with an equivalent amount of fresh buffer. HPLC was utilized to detect the content of released TSN from the TSN-PLGA NPs. The size and charge of TSN-PLGA nanoparticles were measured using dynamic light scattering (DLS) both before incubation and after 36 h of incubation. The DLS data were analyzed with Prism software to compare changes in particle size and charge under different pH conditions.

In vitro *cytotoxicity*

Cytotoxic efficacy of TSN and TSN-PLGA NPs was assessed using the CCK-8 method. CAL27 and HN6 cells were seeded in 96-well plates at a density of 3,000 cells per well, with 15 replicates per group. For each time point (0, 24, 48, 72, and 120 h), three replicates per group were tested (replicates were not reused). Different concentrations of TSN and TSN-PLGA NPs (ranging from 0.001 to 10 μM) were prepared in the cell culture medium, with TSN dissolved in DMSO. After 24 h, 100 μL of the drug solution was added to each well. At the designated time points, 100 μL of the culture medium containing 10% CCK-8 reagent was introduced, and cells were incubated for one hour. Absorbance at 450 nm was measured to determine cell viability (%).

EdU assay

The proliferation ability was evaluated with an EdU assay kit (Uelandy, Shanghai, China, Cat. No C6015S) in accordance with the manufacturer's instructions. After seeding the cells in six-well plates (3×10^6 cells per well), DMSO, 5 nM TSN, 5 nM TSN-PLGA, 10 nM TSN, and 10 nM TSN-PLGA were added to the respective wells. Images were taken under a fluorescence microscope, and we determined the proportion of cells that tested positive for EdU.

Measurement of apoptosis by Annexin V-FITC/PI Assay

CAL27 and HN6 cells (3×10^6 cells per well) were seeded in six-well plates and exposed to TSN and TSN-PLGA NPs (5 nM or 10 nM, TSN-equivalent concentrations) for another 48 h, while phosphate-buffered saline (PBS) was set as control. The cells were then stained with Annexin V-FITC/PI fluorescence detection kit (Uelandy, Shanghai, China, Cat. No F6012L) for 15 min and analyzed by flow cytometry (Becton, Dickinson and Company, LSRFortessaX-20, NJ, USA).

Cell cycle assay

The effect of TSN-PLGA NPs on cell cycle was assessed using a cell cycle and apoptosis kit (Uelandy, Shanghai, China, Cat. No C6031S). HN6 cells were placed in six-well plates (3×10^6 cells per well) and treated with TSN-PLGA NPs (5 nM or 10 nM) for 48 h. Ultimately, the cells were dyed in accordance with the provided guidelines. Flow cytometry was utilized to analyze the distribution of cells in different phases of cell cycle, employing an emission wavelength greater than 535 nm. The distribution of cells in the G0/G1, S, or G2/M phases was assessed by measuring the respective regions.

RNA sequencing analysis

After treating CAL27 and HN6 cell lines with DMSO and TSN for 48 h, RNA was extracted using the Trizol method and transferred to RNA-free EP tubes for storage at −80 °C. Library preparation, sequencing, and data analysis were performed at OE Biotech (Shanghai, China). The remaining samples were kept at −80 °C for subsequent qRT-PCR analysis.

Quantitative reverse-transcription PCR

In accordance with the kit instructions, the extracted RNA was reverse-transcribed. The synthesized cDNA was then diluted tenfold. The following genes were selected for quantitative reverse-transcription PCR reaction: JUN, PCSK9, INHBA, NR4 A1, CDKN1 A, and PLAGL1. The total reaction volume was 20 μL, including 10 μL SYBR Premix Ex Taq II, 1 μL of each forward and reverse primer, 2 μL cDNA, and 7 μL DEPC-H_2O. The PCR program was as follows: 95 °C for 5 min, 98 °C for 10 s, 40 cycles of 60 °C for 30 s, and 72 °C for 10 min. The $2-\Delta\Delta Ct$ method was employed to calculate the relative expression level, with GAPDH serving as the reference gene. Primers used for qPCR are listed in Supplementary Table 1.

Construction of the CDX model

The CDX model was established by injecting an HN6 cell suspension (100 μL) subcutaneously into the right flank of nude mice. Tumor dimensions, namely the length (L) and width (S), were documented every 2 days. Tumor volume was calculated as follows:

$$\text{Tumor volume} = 0.5 \times \text{L} \times \text{S}^2 \quad (3)$$

Upon reaching an average tumor volume of 180 mm^3, the nude mice were randomly divided into four groups: the NS group (normal saline), the 5-FU group (5 mg/kg 5-Fluorouracil), the TSN group (5 mg/kg free Toosendanin), and the TSN-PLGA group (TSN-PLGA nanoparticles, delivering an effective dose of 5 mg/kg TSN). All treatments were administered via intraperitoneal injection. The treatment was given once a week for 2 weeks. 5-FU is a widely used antimetabolite drug in cancer chemotherapy and is also frequently used in chemotherapy for OSCC [32]. Therefore, we chose the 5-FU group as the positive control group in this study.

Construction of the PDX model

To establish the PDX model, fresh tumor tissues were collected from the patient with OSCC of the tongue. The tumor tissues were collected within 30 min of surgical resection, focusing on tumor edges with minimal necrosis. The tissues were then soaked in DMEM culture medium containing 10% FBS and 0.005% penicillin–streptomycin at 4 °C. The tumor tissues were trimmed into 2–3 mm^3 fragments using tissue scissors. The mice were anesthetized with 1% sodium pentobarbital solution (80 mg/kg) via intraperitoneal injection. The trimmed tumor tissues were inserted into the subcutaneous space on the back of the mice (F1). When the volume of the transplanted tumors reached approximately 100 mm^3, the tumor tissues were trimmed into 2–3 mm^3 fragments and transplanted into new BALB/c nude mice (F2). The third-generation nude mice (F3) were constructed using the same method. Hematoxylin–eosin (HE) staining and immunohistochemical staining were performed on the mouse tumor tissues from the PDX model and the original patient tumor tissues to evaluate their homogeneity. When the average tumor volume of the F3 nude mice reached 180 mm^3, they were randomly divided into four treatment groups: the NS group (normal saline), the 5-FU group (5 mg/kg 5-Fluorouracil), the TSN group (5 mg/kg free Toosendanin), and the TSN-PLGA group (TSN-PLGA nanoparticles, containing an effective dose of 5 mg/kg TSN). All treatments were administered via intraperitoneal injection.The treatment was administered once a week for 2 weeks. The mice were observed daily for diet, behavior, and activity. Tumor volume was measured with calipers every 2 days, and the weight and tumor volume of each nude mouse were recorded. A tumor growth curve was plotted based on the data.

Two weeks after the first injection, the nude mice were euthanized by intraperitoneal injection of an excess amount of 1% sodium pentobarbital solution. The tumors were dissected, and their volume was measured. Tumor weight was recorded to calculate the percentage of tumor growth inhibition (TGI) using the following equation:

$$TGI = \left(1 - \frac{\text{average tumor weight of the treatment group}}{\text{average tumor weight of the NS group}}\right) \times 100\% \quad (4)$$

The tumor samples were immersed in a 4% paraformaldehyde solution, embedded in paraffin, and sectioned for subsequent immunohistochemical and TUNEL staining. Additionally, the heart, liver, kidney, and jejunum of the nude mice were collected for HE staining.

HE staining

To assess organ toxicity, we performed HE staining on the tumor tissues and examined the heart, liver, kidney, and jejunum of the nude mice. In short, the tissues were fixed in 4% paraformaldehyde for 24 h, embedded in paraffin, and sectioned. The sections were treated with HE, sealed using neutral resin, observed through an optical microscope, and captured in photographs.

Immunohistochemical staining

The tumor tissues were sectioned and deparaffinized following routine procedures. Antigen retrieval was performed using citrate buffer, and blocking was carried out using goat serum. After an overnight incubation with the primary antibody at 4 °C, the samples were stained with DAB. They were observed and photographed using an optical microscope.

TUNEL staining

Terminal deoxynucleotidyl transferase-mediated nick end labeling (TUNEL) staining was performed on the mouse tumor tissues to provide information about tumor cell apoptosis. TUNEL staining was performed in accordance with the instructions. DAPI staining was subsequently performed, and the slides were finally mounted using an anti-fade mounting medium. The slides were observed and photographed under a fluorescence confocal microscope.

Statistical analysis

Statistical analysis was conducted using GraphPad Prism 9 software (GraphPad, San Diego, CA, USA), employing Student's t-test and one-way analysis of variance (ANOVA). The data are expressed as the mean ± standard error of the mean (SEM). $p < 0.05$ was considered statistically significant.

Results

Preparation and characterization of TSN-PLGA NPs

Figure 1A and B display the chemical structures of TSN and PLGA, respectively. We employed the double emulsion-solvent evaporation method to prepare the TSN-PLGA NPs. The NPs were subsequently freeze-dried for

24 h, which resulted in the formation of a white, loose powder (Fig. 1C). Examination under SEM and TEM (Fig. 1D,E) revealed that the TSN-PLGA NPs exhibited a predominantly spherical particle morphology. The particles demonstrated a relatively uniform size distribution and uniform dispersion, with a size range of approximately 100–200 nm within the observed field. Moreover, we found that the PLGA outer membrane was intact, ensuring complete encapsulation of TSN.

We utilized an Anton Paar particle size and ZP analyzer to investigate the particle size, distribution, and ZP of TSN-PLGA NPs. Particle size was measured by DLS technique. As shown in Fig. 1F, the NPs exhibited a unimodal normal distribution with an average particle size of 135.48 ± 0.37 nm and PDI of (0.05 ± 0.04) %. ZP was − 18.33 ± 1.33 mV (Fig. 1G), suggesting that the particles possessed a negative surface charge—a characteristic that promotes their stability in the bloodstream and potentially extends the duration of drug circulation within the blood. EE and DL of TSN-loaded PLGA-NPs were 88.23% and 1.08%, respectively, as measured using HPLC.

In vitro *drug release curve of TSN-PLGA NPs*

TSN-PLGA nanoparticles were incubated in PBS buffer at pH 5.4 or 7.4 to simulate drug release, with pH 5.4 mimicking the acidic environment of lysosomes in tumor cells and pH 7.4 reflecting the physiological conditions of the human body. As shown in Fig. 1H, the drug exhibited rapid release within the first 6 h, followed by stabilization of the release curve after 12 h. At 36 h, approximately 85.00% of TSN was released in the pH 5.4 group, while about 40.26% was released in the pH 7.4 group. These results demonstrate that TSN-PLGA nanomaterials exhibit excellent drug release performance in an acidic environment. Therefore, it can be anticipated that once these TSN-PLGA NPs enter tumor cells, they can achieve efficient and controlled drug release in the acidic environment of tumor cell lysosomes. As shown in Fig. 1I-M, the DLS results of TSN-PLGA nanoparticles before and after 36 h of incubation are presented. Under the pH 7.4 condition, the charge and particle size of the nanoparticles did not show significant changes, indicating that TSN-PLGA nanoparticles maintain good stability under physiological pH conditions. In contrast, at pH 5.4, both the absolute value of the charge and the particle size of TSN-PLGA nanoparticles significantly decreased, suggesting that the nanoparticles underwent degradation in the acidic environment. Based on these findings, we conclude that the drug release from TSN-PLGA nanoparticles may result from a combined mechanism involving both degradation and charge alteration.

Protein adsorption assay

PLGA enhances protein solubility and plasma stability [33–35]. To evaluate the interaction between nanoparticles and proteins, we used BSA as a model plasma protein. As shown in Fig. 1N, under physiological conditions (pH 7.4), nanoparticles exhibited minimal protein adsorption after 2 h of incubation, with only slight adsorption observed after 4 h. After 36 h under the same conditions, prodrug-based nanoparticles continued to show low protein adsorption, while free TSN exhibited strong protein adsorption. Compared to free TSN, the nanoparticles demonstrated reduced nonspecific protein adsorption, suggesting that nanoparticles may prolong blood circulation time. Therefore, TSN-PLGA nanoparticles represent a promising drug delivery system with enhanced plasma stability.

Analysis of the viability of OSCC cells in vitro

The CCK-8 assay was used to evaluate the viability of CAL27, HN6, and HOEC cells after 48 h of treatment with TSN and TSN-PLGA NPs. The dose–response curves were fitted, and the IC50 values were calculated. As shown in Fig. 2A, the IC50 values of TSN against CAL27 and HN6 cells were 25.7 nM and 16.3 nM, respectively. For TSN-PLGA NPs, the IC50 values against CAL27 and HN6 cells were 8.1 nM and 13.1 nM, respectively. Based on the determined IC50 values for the two drugs, 5 nM and 10 nM concentrations were chosen for the subsequent experiments. As shown in Figure S1, the cell viability of HOEC cells treated with TSN and TSN-PLGA NPs for 48 h was not significantly different from that of the control. Preliminarily, this finding indicated negligible toxicity of the drugs on HOEC cells.

(See figure on next page.)

Fig. 1 Characterization and the in vitro drug release profile of TSN-PLGA NPs. **A** The chemical structure of TSN. **B** The chemical structure of PLGA. **C** Appearance of TSN-PLGA NPs lyophilized powder. **D** SEM image of TSN-PLGA NPs. **E** TEM image of TSN-PLGA NPs. **F** Particle size distribution of TSN-PLGA NPs ($n = 3$). **G** Zeta potential distribution of TSN-PLGA NPs ($n = 3$). (H) The cumulated release curve of TSN from TSN-PLGA NPs in PBS (pH 5.4 or 7.4, $n = 3$). (I) Zeta potential distribution of TSN-PLGA NPs at 0 h ($n = 3$). (J-K) Zeta potential distribution of TSN-PLGA NPs at 36 h (PBS, pH = 5.4 or 7.4, $n = 3$). (L-M) Particle size distribution of TSN-PLGA NPs at 0 h and TSN-PLGA NPs at 36 h (PBS, pH = 7.4 or 5.4, $n = 3$). (N) Protein adsorption of nanoparticles and free TSN was measured after incubation at 37 °C (pH 7.4) for different time intervals, with BSA as the standard (mean ± SD, $n = 3$)

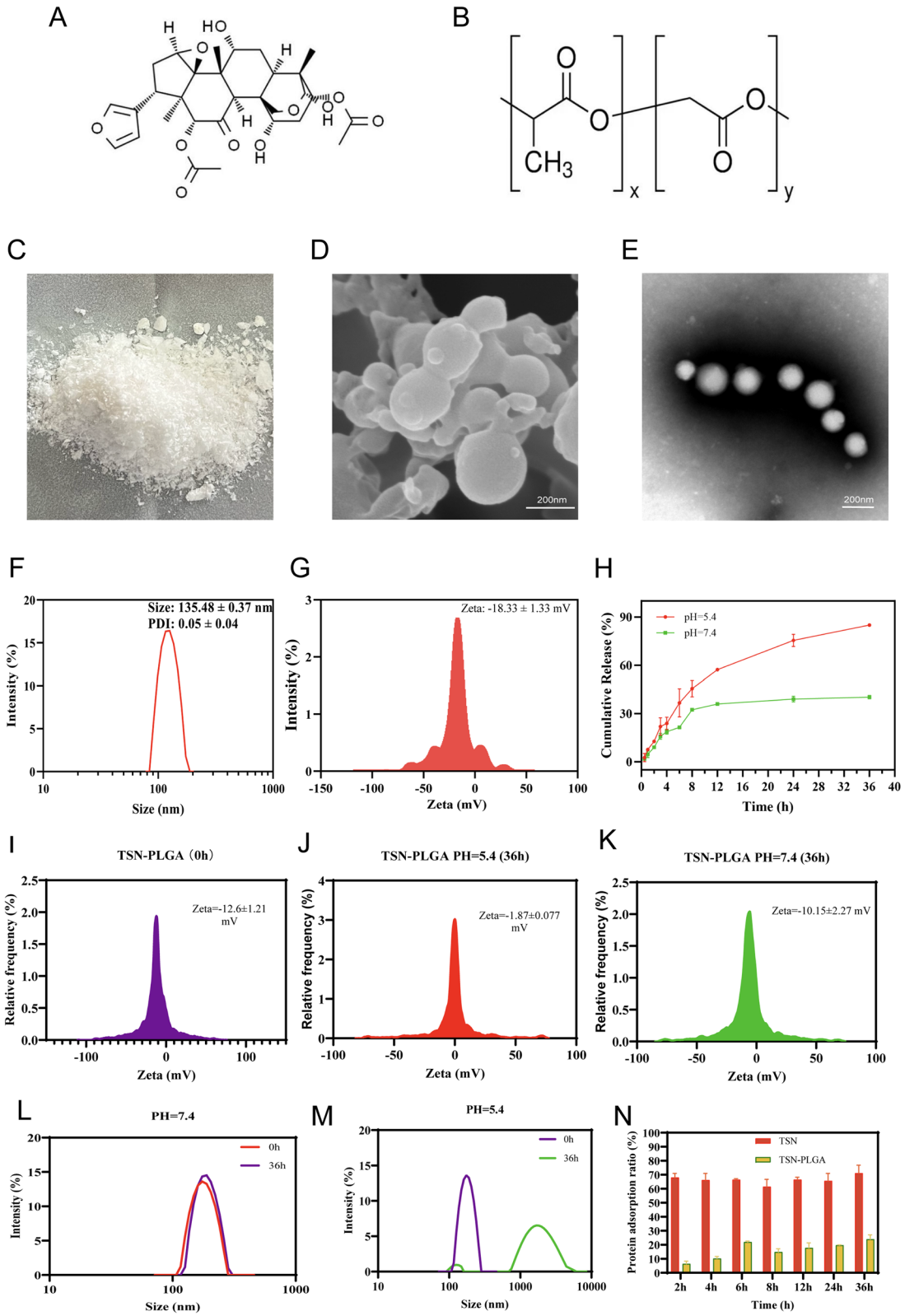

Fig. 1 (See legend on previous page.)

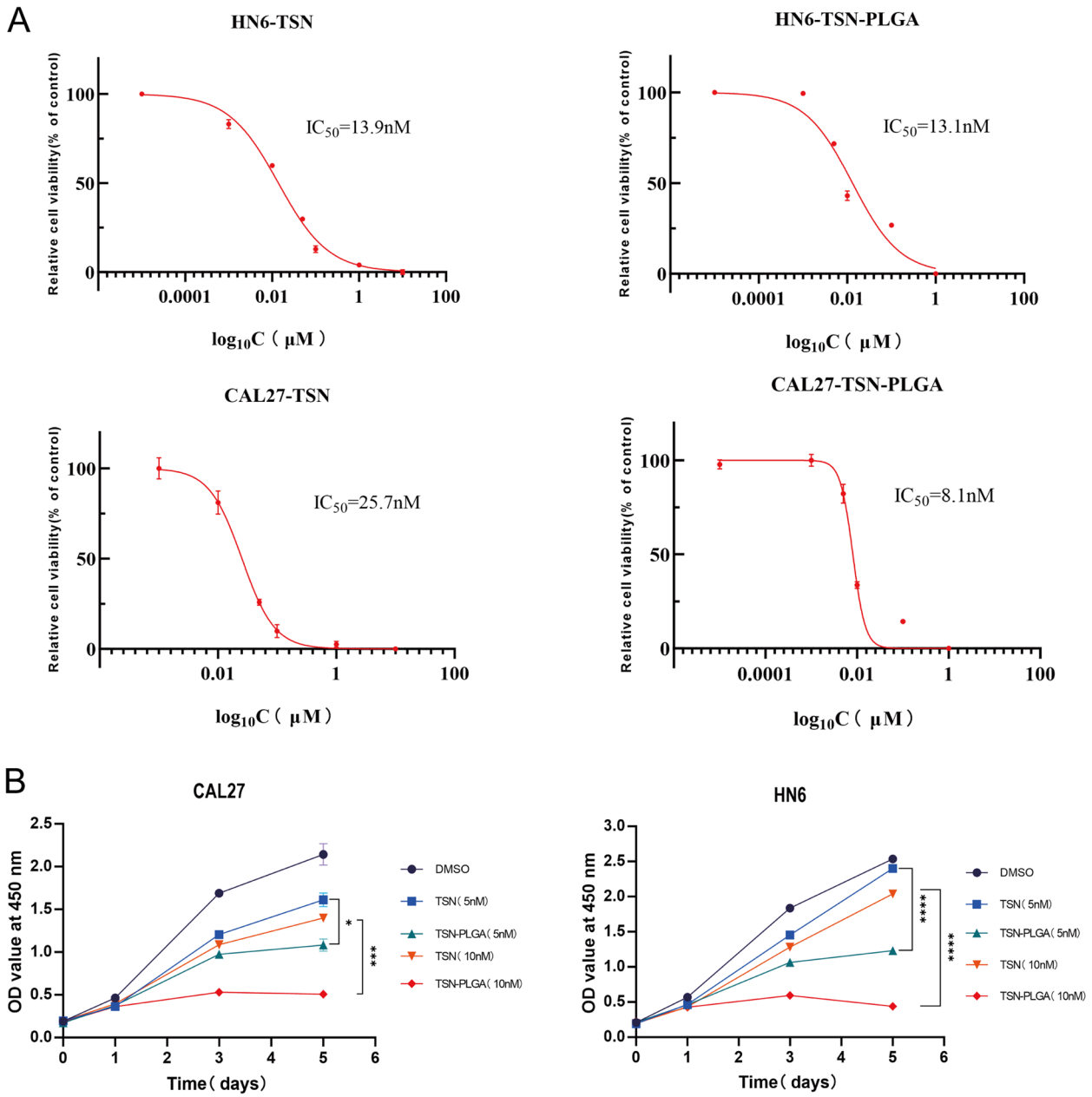

Fig. 2 CCK-8 assay for cell viability. **A** Fitting curves of cell viability after 48 h of treatment with TSN and TSN-PLGA NPs. **B** CCK-8 assay to detect changes in cell proliferation ability of CAL27 and HN6 cells treated with drugs ($n = 3$). * $p < 0.05$, **** $p < 0.0001$

To investigate the effects of TSN and TSN-PLGA NPs on OSCC cell proliferation, we performed CCK-8 assays on the cells treated with two different concentrations (5 nM and 10 nM) of TSN and TSN-PLGA NPs. We found significant disparities in cell proliferation after 3 days between the treatment groups and the DMSO group. Significant variations in cell proliferation were also noticed between the treatment groups and the DMSO group (Fig. 2B) following a 5-day culture period. The proliferation activity of OSCC cells decreased with time, and the concentration of TSN and TSN-PLGA NPs increased within a certain range. In both CAL27 and HN6 cells, the suppressive effect of TSN-PLGA NPs on OSCC cell growth surpassed that of TSN, with 5 nM TSN-PLGA NPs exhibiting a stronger inhibitory effect than 10 nM TSN. These findings preliminarily indicate the drug release properties of TSN-PLGA NPs.

EdU assay

The EdU assay is used to directly detect the proliferation of live cells. This method enables rapid detection of cell proliferation and provides a more accurate reflection of the cell proliferation status. The results (Fig. 3) demonstrated a significant decrease in cell proliferation capacity of CAL27 and HN6 cells after the treatment with TSN and TSN-PLGA NPs. The inhibitory effect increased with the increase in drug concentration. The cell proliferation capacity of OSCC cells treated with 10 nM TSN-PLGA NPs was significantly weaker than that of the cells treated with 10 nM TSN (CAL27: $p < 0.05$; HN6: $p < 0.01$). These preliminary findings suggest that both TSN and TSN-PLGA NPs have the ability to inhibit OSCC cell proliferation, but TSN-PLGA NPs exhibit stronger inhibitory effects than TSN.

Induction of S-phase cell cycle arrest and apoptosis in OSCC

Apoptosis is one of the most common mechanisms of cancer cell death. To investigate whether TSN and TSN-PLGA NPs can induce apoptosis in OSCC cells, different concentrations of TSN and TSN-PLGA NPs were used to treat CAL27 and HN6 cells for 48 h, followed by Annexin V-PI staining and flow cytometry analysis. Figure 4A showed that the level of apoptosis of CAL27and HN6 cells increased to varying degrees after the treatment with TSN and TSN-PLGA NPs, but TSN-PLGA NPs exhibited a stronger ability to promote apoptosis at the same concentration.

It has been suggested that TSN may participate in the regulation of crucial processes such as cell cycle, thereby affecting tumor occurrence and development [14]. Therefore, to examine the effects of TSN-PLGA NPs on cell cycle of OSCC cells and the differences among the groups, we used propidium iodide DNA staining and flow cytometry to detect cell cycle arrest. As shown in Fig. 4B, in HN6 cells, the percentage of cells in S phase after the treatment with 5 nM and 10 nM TSN-PLGA NPs was(26.3 ±0.7)%, and (27.2 ±1.95)%, respectively, which was significantly higher than that in the control group (19.2 ± 2.97)% ($p < 0.05$). These results indicate that TSN-PLGA NPs might induce apoptosis of HN6 cells by slowing down the progression of cells through S phase.

RNA sequencing analysis and validation

To investigate the inhibitory mechanism of TSN on the proliferation of OSCC cells, we performed a 48-h

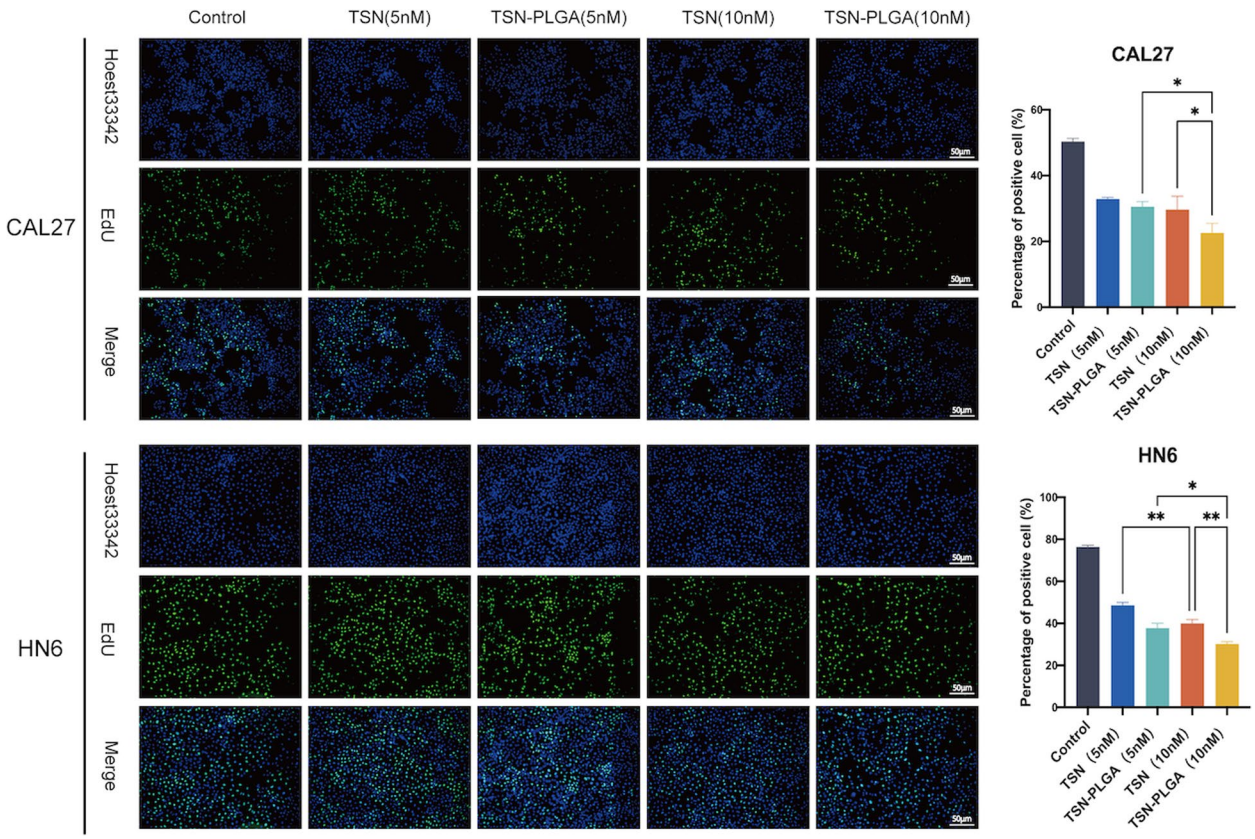

Fig. 3 EdU assay to detect changes in cell proliferation ability of CAL27 and HN6 cells treated with drugs (scale bar = 50 μm). * $p < 0.05$, ** $p < 0.01$

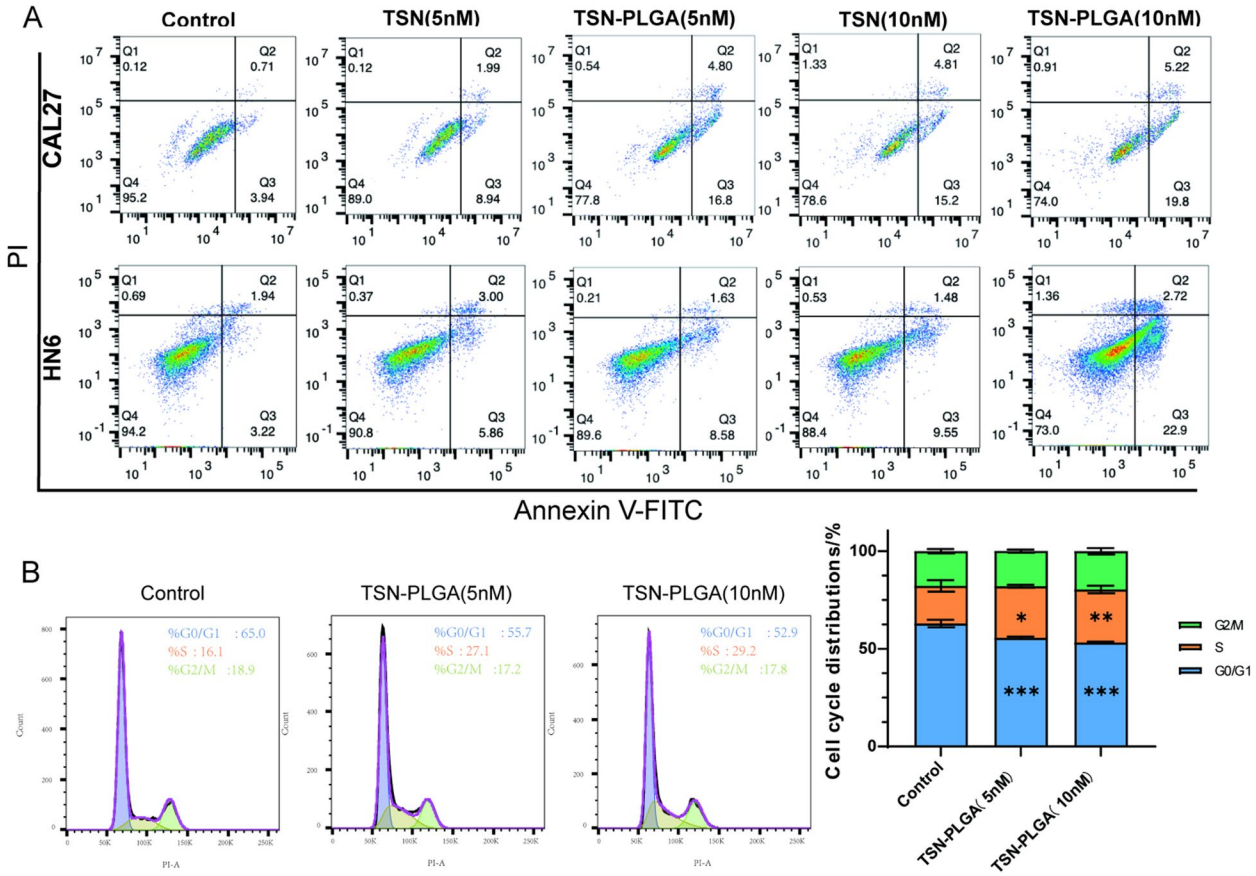

Fig. 4 TSN and TSN-PLGA NPs induce S-phase cell cycle arrest and promote apoptosis in OSCC cells. **A** The apoptotic activity of CAL27 and HN6 cells after treatment with drugs for 48 h. The cells were stained by AnnexinV and PI and analyzed by flow cytometry. **B** The cell cycle distribution of HN6 cells after treatment with TSN-PLGA NPs for 48 h ($n = 3$). * $p < 0.05$ compared with the control group

treatment of OSCC cells with TSN. Subsequently, the Trizol method was employed to extract total RNA for RNA-sequencing analysis. Through differential gene enrichment analysis, the HN6 cell line showed a total of 965 differentially expressed genes (DEGs), namely 573 upregulated and 392 downregulated genes. The CAL27 cell line had a total of 3124 DEGs, namely 1563 upregulated and 1561 downregulated genes (Fig. 5A). Figure 5B shows the shared and unique DEGs between the HN6 and CAL27 cell lines. In total, 487 DEGs were shared between the cell lines. Additionally, a volcano plot was generated for all genes that met the criteria of $p < 0.05$ and |log2(fold change)|> 1 to visualize the differential gene expression between the two groups. As shown in Fig. 5C, the volcano plot depicts the distribution of DEGs between the TSN group and the DMSO group, with red and blue indicating significantly upregulated and downregulated DEGs, respectively. We next conducted KEGG pathway enrichment analysis of the identified DEGs. Figure 5D shows the 20 most significantly enriched pathways. Specifically, the DEGs were highly enriched in pathways such as JAK–STAT, MAPK, and PI3 K–Akt, with a relatively high number of genes, indicating their potential involvement in the mechanisms affected by TSN treatment.

We used gene set enrichment analysis (GSEA) to evaluate whether predefined gene sets showed statistically significant differences between the DMSO and TSN groups, so as to identify important pathways from the overall gene expression matrix. As shown in Fig. 5E, there was a dense distribution of core genes in the gene set of the JAK/STAT pathway of interest, displaying a consistently high expression trend. Thus, we identified a gene set with consistently different expression patterns in this pathway, providing a research direction for investigating the mechanism of TSN's effect on OSCC cells.

The DEGs identified through RNA sequencing are shown in Fig. 5F as a heat map. We performed qPCR validation of these genes in CAL27 cells after DMSO and TSN treatment, as shown in Fig. 5G. In the TSN group, the expression levels of JUN, PCSK9, INHBA, NR4 A1, CDKN1 A, and PLAGL genes were

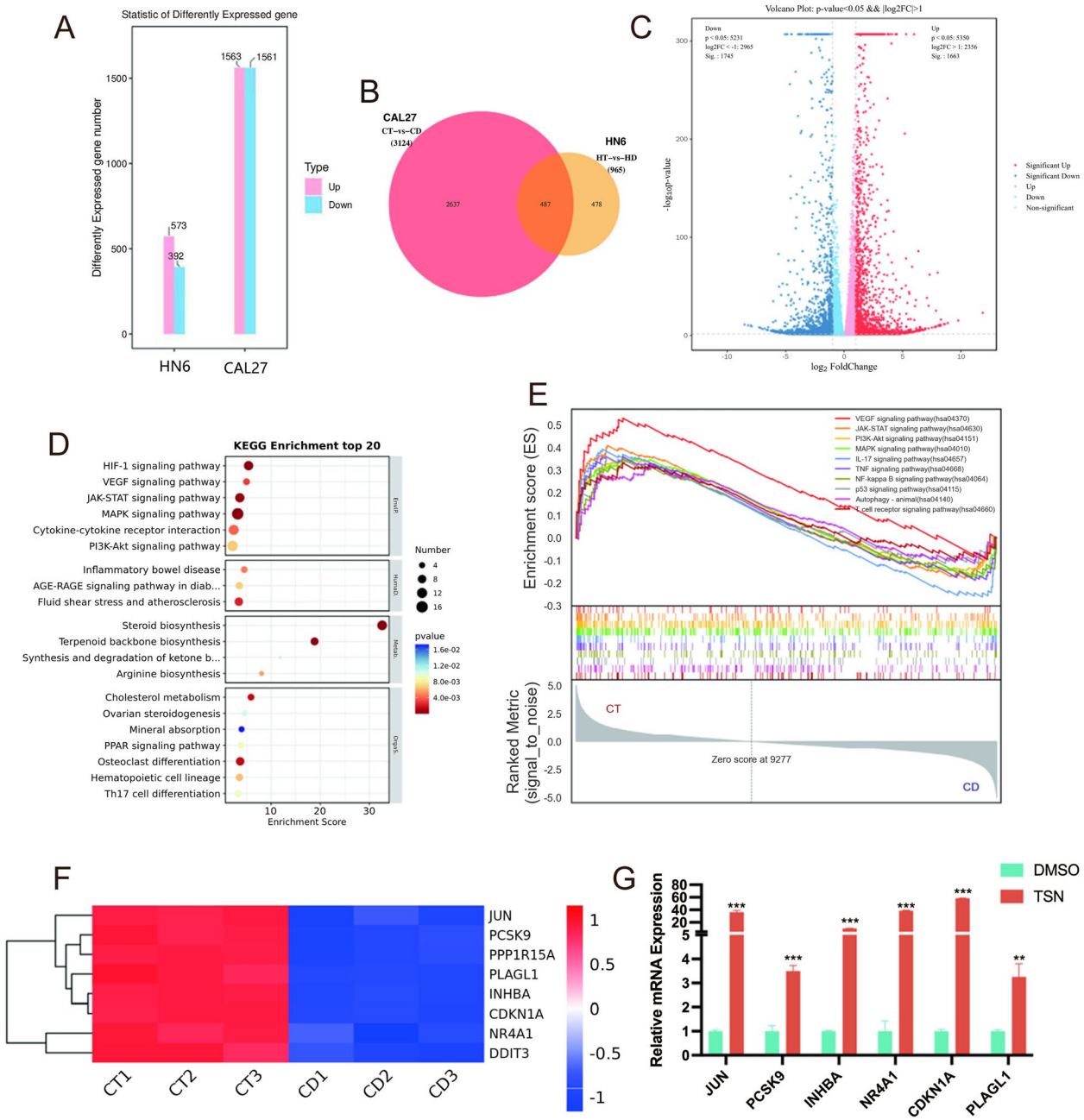

Fig. 5 RNA-sequencing analysis and validation of qPCR. **A** Total number of DEGs. **B** Shared and unique expressed genes between CAL27 and HN6 cell lines. **C** DEGs volcano plot. **D** Bubble plot of KEGG enrichment analysis. **E** GSEA plot. **F** Heat map of DEGs. **G** Validation of genes expression after DMSO and TSN treatment in CAL27 cells. ** $p < 0.01$, *** $p < 0.001$ compared with the DMSO group

significantly higher than those in the DMSO group. The qPCR results were consistent with the RNA-sequencing results, indicating the high reliability of the RNA-sequencing analysis. Moreover, JUN and PCSK9 genes are key genes that promote cell apoptosis, while INHBA, NR4 A1, CDKN1 A, and PLAGL1 genes are closely associated with cell cycle arrest. These experimental results further suggest that TSN may inhibit tumor cell growth by upregulating apoptosis-related genes and interfering with cell cycle regulation.

TSN and TSN-PLGA NPs regress tumor growth of OSCC in the CDX model

The aforementioned in vitro experimental results indicate that both TSN and TSN-PLGA NPs possess the capability to hinder the proliferation and promote apoptosis of OSCC cells. Hence, to further investigate the effectiveness and safety of TSN and TSN-PLGA NPs in vivo, the CDX tumor model was established.

In the CDX model, there were no deaths, infections, or signs of toxicity during the treatment period in the different groups of nude mice. There were no obvious changes in the body weight of the nude mice among the three treatment groups compared with the NS group (Fig. 6B). As shown in Fig. 6C, both the TSN group and TSN-PLGA NPs group exhibited superior tumor-suppression effects relative to the 5-FU group ($p < 0.001$), but the TSN-PLGA NPs group demonstrated a more pronounced tumor-inhibitory effect than the TSN group ($p < 0.05$).

After the completion of the experimental period, the tumors were extracted and weighed (Fig. 6A and D). Then, TGI was calculated, and the percentage of TGI was 41.17%, 58.82%, and 64.70% for the 5-FU, TSN, and TSN-PLGA groups, respectively. These results were consistent with the tumor volume findings, collectively indicating that TSN and TSN-PLGA NPs have a greater ability to inhibit tumor growth than 5-FU.

Next, we performed HE staining and Ki-67 immunohistochemical staining of the tumor tissues from the CDX model (Fig. 6E). In the NS group, most tumor cells exhibited nuclear pleomorphism, indicating a significant degree of dedifferentiation. The NS group had the highest percentage of Ki-67–positive cells, suggesting that the tumor cells were in a rapidly proliferating stage. As shown in Fig. 6F, the TSN-PLGA NPs group exhibited a lower proportion of Ki-67–positive cells than did the other groups. Our results suggest that both TSN and TSN-PLGA NPs exhibit antitumor properties, but TSN-PLGA NPs demonstrate superior efficacy.

TUNEL expression level was examined to determine the degree of apoptosis in OSCC cells. As shown in Fig. 6G, the TSN-PLGA NPs group displayed extensive areas with intense red fluorescence signals, possibly reflecting the presence of clustered apoptotic cells. As shown in Fig. 6H, the TSN-PLGA NPs group showed a higher proportion of cells undergoing apoptosis than did the other groups. These results imply that both TSN and TSN-PLGA NPs possess the capacity to induce apoptosis in tumor cells to a certain extent.

There were no significant changes in cardiac myocytes, liver sinusoids, renal glomeruli, intestinal glands, and other morphological structures (Figure S2). These findings demonstrated that TSN and TSN-PLGA NPs at a dose of 5 mg/kg did not exhibit significant toxic side effects on the vital organs of the mice, demonstrating potential biological safety.

Further investigation of the inhibitory effects of TSN and TSN-PLGA NPs on OSCC in the PDX model

Based on the aforementioned in vivo studies via the CDX model, we further constructed the PDX model—which better simulates the tumor microenvironment—to further validate the therapeutic effects of the two drugs on OSCC. The original tumor tissue was obtained from a 58-year-old man diagnosed with high-grade squamous cell carcinoma of the tongue ($T_3N_0M_0$). The fresh surgical specimen of the primary lesion was trimmed into 2–3 mm^3 tissue fragments and implanted into the first-generation nude mice (F1). The tumor formation time in the F1 mice was 45 days. Subsequently, the tumor tissue from F1 was transplanted into other nude mice (F2), and the tumor formation time in the F2 mice was 30 days. Finally, the tumor tissue from F2 was transplanted into the third-generation nude mice (F3), and the tumor formation time in the F3 mice was approximately 28 days (Fig. 7A). We performed HE staining and immunohistochemical (IHC) staining for CK56, Ki-67, P16, and P53 on both the patient's primary tumor tissue and the tumor tissue from the F3 nude mice to confirm the homogeneity of the xenograft model (Figure S3). The results showed a high degree of consistency between the constructed PDX model and the primary tumor derived from the patient.

Similarly, there were no notable changes in body weight among the treatment groups during the entire dosing period relative to the NS group (Fig. 7C). After a 2-week period of intraperitoneal injections, the tumor tissues were dissected (Fig. 7B). According to the tumor volume growth curves (Fig. 7D), all treatment groups exhibited inhibitory effects on OSCC growth, but TSN-PLGA NPs showed the strongest effect. The percentage of TGI in the 5-FU, TSN, and TSN-PLGA groups was 30.48%, 50.34%, and 66.10%, respectively. Consistent conclusions were drawn regarding tumor weight (Fig. 7E). The results of IHC staining (Fig. 7F) showed that the TSN-PLGA NPs group exhibited lower Ki-67 expression than did the other groups ($p < 0.05$) (Fig. 7G). Aberrant activation of STAT3, indicated by increased levels of p-STAT3, is often observed in OSCC tissues. As shown in Fig. 7H, there was no difference between the NS group and the 5-FU group in p-STAT3 expression. However, the TSN group and the TSN-PLGA NPs group exhibited notably reduced levels of p-STAT3 expression in comparison to the 5-FU group ($p < 0.01$). Our results revealed that TSN and TSN-PLGA NPs have the potential to greatly decrease the levels of p-STAT3 in OSCC tissues. Furthermore, as shown in the TUNEL cell apoptosis assay (Fig. 7I), both

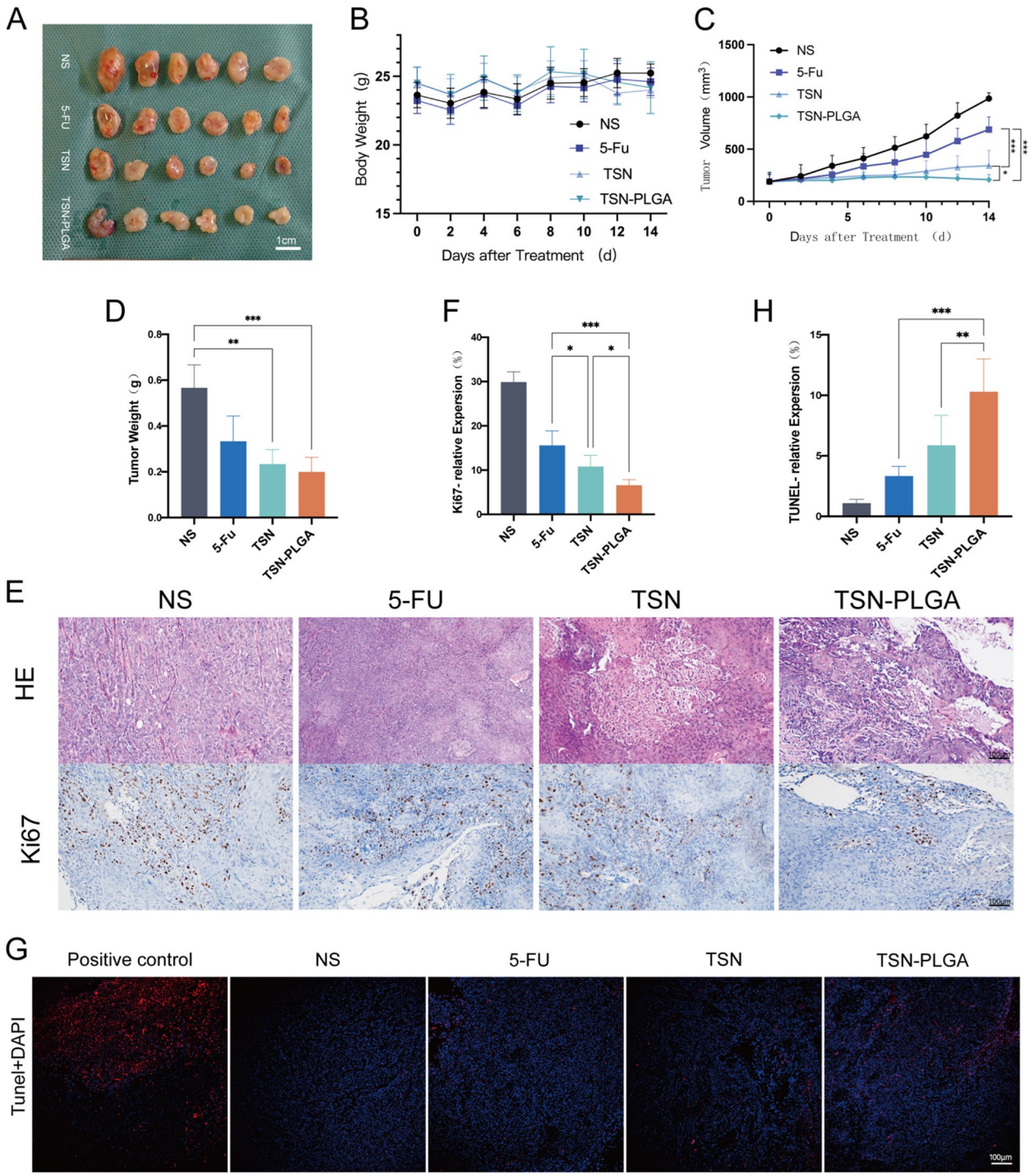

Fig. 6 TSN and TSN-PLGA NPs regress tumor growth of OSCC in the CDX model. **A** Comparison of tumor tissue in nude mice ($n = 6$). **B** Body weight change curves of nude mice. **C** Tumor volume growth curves of nude mice. **D** Comparison of tumor weight in nude mice. **E**–**F** HE staining and effect of drug on the expression of Ki-67 in tumor of nude mice (scale bar = 100 μm). **G**– **H** TUNEL staining of tumor tissues in nude mice (scale bar = 100 μm). * $p < 0.05$, ** $p < 0.01$, *** $p < 0.001$

TSN and TSN-PLGA NPs have the ability to promote tumor cell apoptosis. Additionally, TSN-PLGA NPs may have a stronger effect in promoting OSCC apoptosis than TSN alone (Fig. 7J). HE staining of vital organs in all of the groups of nude mice showed no significant organ changes, suggesting that the drugs administered at a dosage of 5 mg/kg exhibited a considerable degree of safety (Figure S4).

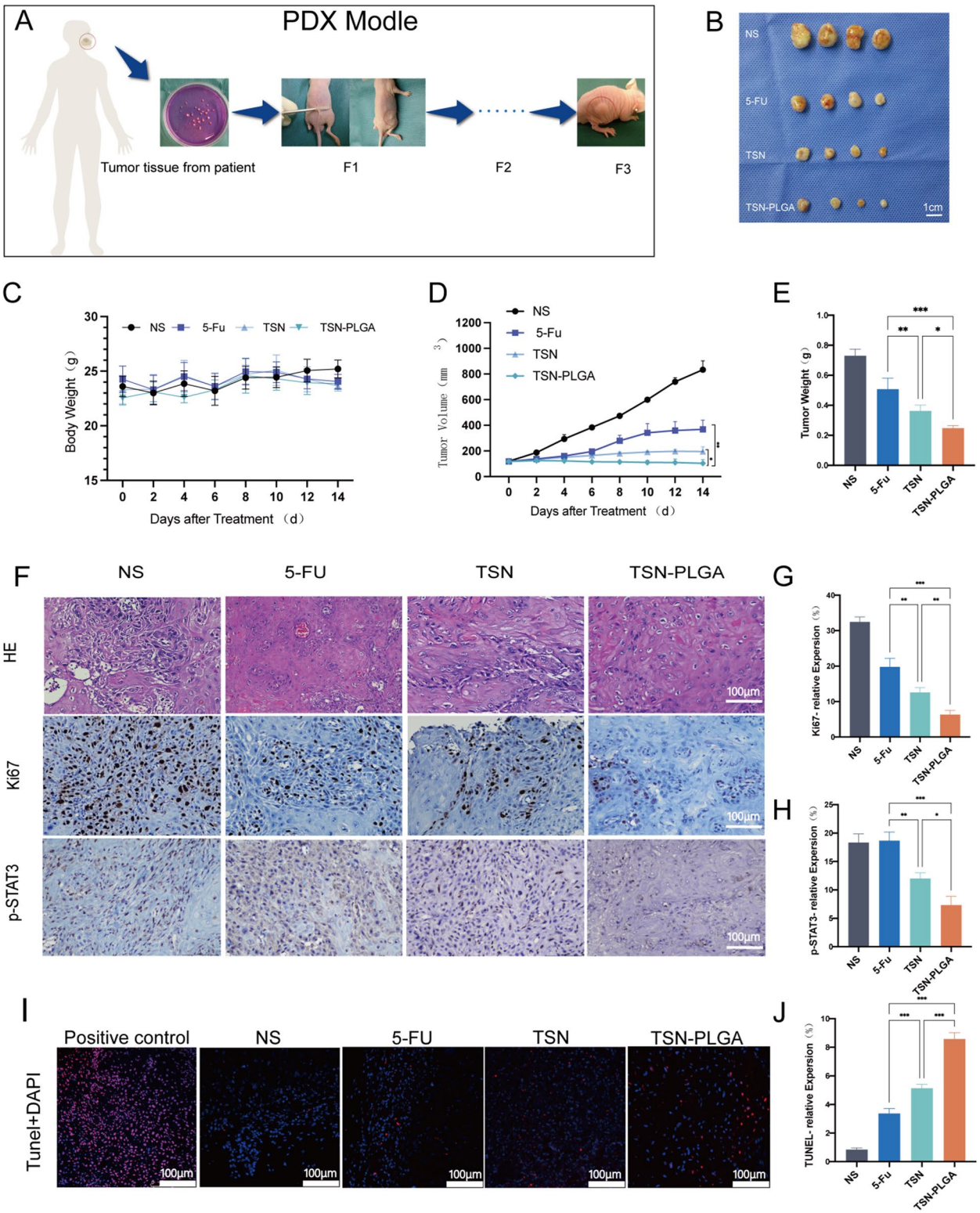

Fig. 7 TSN and TSN-PLGA NPs regress tumor growth of OSCC in the PDX model. **A** The PDX model construction method. **B** Comparison of tumor tissue in nude mice ($n = 4$). **C** Body weight change curves of nude mice $n = 4$. **D** Tumor volume growth curves of nude mice ($n = 4$). **E** Comparison of tumor weight in nude mice ($n = 4$). **F**– **H** HE staining and effect of drug on the expression of Ki-67 and p-STAT3 in tumors of nude mice ($n = 4$, scale bar = 100 μm). **I**–**J** TUNEL staining and expression of tumor tissues in nude mice ($n = 4$,scale bar = 100 μm). * $p < 0.05$, ** $p < 0.01$, *** $p < 0.001$

Discussion

OSCC has become a significant public health issue due to its aggressive nature and high metastatic potential. It is associated with negative effects on patients'survival time and quality of life. Patients diagnosed with advanced OSCC have a survival rate below 30% [36]. Therefore, it is crucial to explore novel and effective treatment strategies to complement current therapies for OSCC. The utilization of natural bioactive compounds found in herbs is a promising option for improving treatment efficiency and reducing adverse effects. As a promising anticancer agent, herb-extracted TSN has been demonstrated to exhibit antiproliferative activity against various tumor cell lines in vitro [37–39]. However, TSN itself has low water-solubility and bioavailability, and exhibits certain hepatotoxicity [40]. In previous studies, numerous drugs derived from natural herbs, such as atropine, scopolamine, paclitaxel, and camptothecin, have been used. Nevertheless, although these drugs initially displayed some side effects, they have found extensive use in clinical treatment following chemo- or nano-modification, which served as a source of inspiration for us [41]. Hence, considering the potent anticancer capabilities of TSN and aiming to address these limitations, we employed PLGA encapsulation (TSN-PLGA NPs) to improve the water-solubility and efficacy of the TSN.

It has been shown that nanomedicines with particle sizes ranging from 100 to 200 nm exhibit optimal enhanced permeability and retention (EPR) effect [42]. The EPR effect can effectively utilize the physiological characteristics and structural differences of tumor tissues, allowing large molecular substances to be efficiently targeted and distributed in tumor tissues, thereby improving the treatment efficacy and reducing adverse reactions [43]. TSN-PLGA NPs had a particle size of 135.48 ± 0.37 nm, which could enable drug accumulation in tumor tissues via EPR effect. The characterization of TSN-PLGA NPs demonstrated that the nanocarrier particles prepared in our study had appropriate particle size, uniform dispersion, system stability, and sustained release behavior.

Our study showed that both TSN and TSN-PLGA NPs exhibit anticancer effects by inhibiting the survival and proliferation of OSCC cells. Additionally, they both induce apoptosis and cause S-phase cell cycle arrest. These results are in accordance with a previous study, which showed that TSN dose-dependently induced colorectal cancer cell cycle arrest in S phase [15]. TSN and TSN-PLGA NPs exhibit selective cytotoxicity against OSCC, as they can inhibit the growth of OSCC cells at lower concentrations without affecting HOEC viability.

In addition, we found that TSN and TSN-PLGA NPs had superior antitumor effects than 5-FU after absorption and metabolism in both the CDX and PDX models. The results were consistent with the in vitro experiments, as no significant adverse side effects were found in the mice after treatment. Histological examination of the liver tissue revealed no apparent pathological changes in the nude mice. According to experimental work in mice by Yang et al. [37], administering 10 mg/kg TSN by intraperitoneal injection can cause severe liver damage, with elevated Alanine Aminotransferase/Aspartate Transaminase (ALT/AST) activity and typical histopathological changes in the liver. This provides a reference basis for our animal experiments. In our study, the dosage of intraperitoneally injected TSN (5 mg/kg) was relatively safe. Furthermore, the modification of TSN with PLGA resulted in TSN-PLGA NPs that possessed passive tumor-targeting capabilities and exhibited enhanced biosafety.

From the analysis of RNA-sequencing data, we may infer that TSN hinders the progression of OSCC and promotes apoptosis by activating signaling pathways such as JAK/STAT and PI3 K–Akt. The JAK/STAT and PI3 K–Akt signaling pathways play a crucial role in tumor formation, engaging in diverse biological activities such as cellular proliferation, metabolism, survival, and apoptosis [44, 45]. The STAT family is a group of signal transducers and transcription activators that can bind to DNA. Phosphorylation of STAT3 can lead to significant activation of the JAK/STAT3 pathway, thereby promoting cell proliferation. It has been reported that STAT3 is highly expressed in tumor tissues of OSCC and has a significant effect on invasion [46]. The study by Yang et al. demonstrated that TSN inhibited liver cancer metastasis by activating the tumor suppressor gene WWOX and suppressing the JAK/STAT3 signaling pathway [47]. Furthermore, Zhang et al. [48] demonstrated that TSN directly bound to the SH2 domain of STAT3, inhibiting the phosphorylation of STAT3.

The activation of the PI3 K/Akt pathway can increase the proliferation of tumor cells by regulating cell cycle regulatory factors and promoting protein synthesis. Additionally, Akt activation enables tumor cells to evade apoptosis [49]. The study conducted by Zhang et al. [50] observed that TSN effectively suppressed the phosphorylation of PI3 K, Akt, and mTOR proteins in glioma cells. Furthermore, the inhibitory effect of TSN on glioblastoma was reversed by PI3 K activators. Additionally, another study has shown that TSN can reverse the resistance of breast cancer cells to doxorubicin by inhibiting doxorubicin-induced Akt phosphorylation [16]. Therefore, TSN may have great potential as a PI3 K and STAT3 phosphorylation inhibitor for the treatment of OSCC.

Conclusions

In this study, we prepared TSN-PLGA NPs that met the requirements of EPR effect, with appropriate particle size and ZP. The modified TSN-PLGA NPs exhibited significantly enhanced effects on OSCC cells compared with free TSN. The findings from the experiments conducted in vitro and in vivo demonstrated that both TSN and TSN-PLGA NPs effectively inhibited the proliferation of OSCC cells, promoted apoptosis, and induced cell cycle arrest in S phase. RNA sequencing analysis showed that TSN might regulate OSCC cells through the JAK/STAT and PI3 K/Akt signaling pathways. TSN and TSN-PLGA NPs significantly inhibited the growth of OSCC at a dose of 5 mg/kg, showing no apparent toxicity in nude mice and demonstrating potential biocompatibility. In conclusion, TSN delivered and encapsulated by PLGA might serve as an effective anticancer agent for OSCC. Nevertheless, this study does have certain limitations, and further research is warranted to delve into the mechanisms of TSN in OSCC treatment.

Supplementary Information

The online version contains supplementary material available at https://doi.org/10.1186/s12906-025-04957-0.

Supplementary Material 1: Table S1. Primer sequences for JUN, PCSK9, INHBA, NR4 A1, CDKN1 A, PLAGL1; Figure S1. Cell viability after 48 hours of drug treatment of Human normal oral epithelial cells (HOEC); Figure S2. HE staining results of nude mouse heart, liver, kidney, spleen, lung and jejunum tissue sections in CDX model (scale bar=100μm); Figure S3. Immunohistochemical (IHC) and HE results of the primary tumor and the PDX tumor(scale bar=100μm); Figure S4. HE staining results of nude mouse heart, liver, kidney, spleen, lung and jejunum tissue sections in PDX model(scale bar=100μm); Figure S5. Figure S5. Standard curve of TSN; Figure S6. The HPLC Spectrum of TSN.

Acknowledgements

The authors would like to thank Junjin Lin from Public Technology Service Center (Fujian Medical University, Fuzhou, China) for the technical assistance of flow cytometry. We thank LetPub for its linguistic assistance during the preparation of this manuscript.

Authors' contributions

L.C. and C.F. contributed equally to this work. Conceptualization, Y.W. and L.L.; Formal analysis, Y.W., and L.C.; Investigation, Y.W., L.C., and C.F.; Funding acquisition, Y.W.; Methodology, Y.W., L.C., C.F., Z.S., J.W., T.W., D.Z. and L.L.; writing—original draft preparation, L.C. and C.F.; writing—review and editing, Y.W., L.C., C.F., Z.S., J.W., T.W.,Y.W and L.L. All authors have read and agreed to the published version of the manuscript.

Funding

This research was supported by Fujian Provincial Department of Finance [Grant No. 22SCZZX010 and 2023 SCZZX04] and Fujian Provincial Health Technology Project [Grant No.2020CXB031].

Data availability

The datasets used and analyzed during the current study are available from the corresponding author on reasonable request. The RNA-seq data is publicly available at the NCBI Sequence Read Archive (http://www.ncbi.nlm.nih.gov/sra/) with the accession number PRJNA1243870.

Declarations

Ethics approval and consent to participate

The part about tumor tissue of this study was conducted in accordance with the Declaration of Helsinki and approved by all methods were carried out in accordance with relevant guidelines and regulations and were approved by the Ethics Committee of Fujian Medical University (Approval Number: FJMU-IACUC 2022–017). The written informed cosnent was obtained from the participants.The animal study protocol was approved by the Ethics Committee of Fujian Medical University (Approval Number: FJMU-IACUC 2023–0041). The study is reported in accordance with ARRIVE guidelines.

Consent for publication

Not applicable.

Competing interests

The authors declare no competing interests.

Received: 23 April 2024 Accepted: 30 May 2025
Published online: 02 July 2025

References

1. Chi AC, Day TA, Neville BW. Oral cavity and oropharyngeal squamous cell carcinoma–an update. CA Cancer J Clin. 2015;65(5):401–21. https://doi.org/10.3322/caac.21293.
2. Gormley M, Dudding T, Sanderson E, Martin RM, Thomas S, Tyrrell J, Ness AR, Brennan P, Munafo M, Pring M, et al. A multivariable Mendelian randomization analysis investigating smoking and alcohol consumption in oral and oropharyngeal cancer. Nat Commun. 2020;11(1):6071. https://doi.org/10.1038/s41467-020-19822-6.
3. Siegel RL, Miller KD, Wagle NS, Jemal A. Cancer statistics, 2023. CA Cancer J Clin. 2023;73(1):17–48. https://doi.org/10.3322/caac.21763.
4. Sasahira, T.; Kirita, T. Hallmarks of cancer-related newly prognostic factors of oral squamous cell carcinoma. Int J Mol Sci 2018, 19 (8). https://doi.org/10.3390/ijms19082413.
5. Chinn SB, Myers JN. Oral cavity carcinoma: current management, controversies, and future directions. J Clin Oncol. 2015;33(29):3269–76. https://doi.org/10.1200/JCO.2015.61.2929.
6. Cohen EEW, Bell RB, Bifulco CB, Burtness B, Gillison ML, Harrington KJ, Le QT, Lee NY, Leidner R, Lewis RL, et al. The Society for Immunotherapy of Cancer consensus statement on immunotherapy for the treatment of squamous cell carcinoma of the head and neck (HNSCC). J Immunother Cancer. 2019;7(1):184. https://doi.org/10.1186/s40425-019-0662-5.
7. Johnson DE, Burtness B, Leemans CR, Lui VWY, Bauman JE, Grandis JR. Head and neck squamous cell carcinoma. Nat Rev Dis Primers. 2020;6(1):92. https://doi.org/10.1038/s41572-020-00224-3.
8. Ma L, Zhang M, Zhao R, Wang D, Ma Y, Li A. Plant natural products: promising resources for cancer chemoprevention. Molecules. 2021;26:933. https://doi.org/10.3390/molecules26040933.
9. Shi YL, Li MF. Biological effects of toosendanin, a triterpenoid extracted from Chinese traditional medicine. Prog Neurobiol. 2007;82(1):1–10. https://doi.org/10.1016/j.pneurobio.2007.02.002.
10. Jia X, Wang P, Huang C, Zhao D, Wu Q, Lu B, Nie W, Huang L, Tian X, Li P, et al. Toosendanin targeting eEF2 impedes Topoisomerase I & II protein translation to suppress esophageal squamous cell carcinoma growth. J Exp Clin Cancer Res. 2023;42(1):97. https://doi.org/10.1186/s13046-023-02666-5.
11. Liu Y, Zhang X, Liu Z, Huang L, Jia W, Lian X, Weng C, Zhang G, Qi W, Chen J. Toosendanin suppresses African swine fever virus replication through upregulating interferon regulatory factor 1 in porcine alveolar macrophage cultures. Front Microbiol. 2022;13:970501. https://doi.org/10.3389/fmicb.2022.970501.
12. Zhang S, Dong Y, Chen X, Tan CSH, Li M, Miao K, Lu JH. Toosendanin, a late-stage autophagy inhibitor, sensitizes triple-negative breast cancer to irinotecan chemotherapy. Chin Med. 2022;17(1):55. https://doi.org/10.1186/s13020-022-00605-8.

13. Shao S, Li S, Liu C, Zhang W, Zhang Z, Zhu S, Feng Y, Pan Y. Toosendanin induces apoptosis of MKN-45 human gastric cancer cells partly through miR-23a-3p-mediated downregulation of BCL2. Mol Med Rep. 2020;22:1793–802. https://doi.org/10.3892/mmr.2020.11263.
14. He Y, Wang J, Liu X, Zhang L, Yi G, Li C, He X, Wang P, Jiang H. Toosendanin inhibits hepatocellular carcinoma cells by inducing mitochondria-dependent apoptosis. Planta Med. 2010;76(13):1447–53. https://doi.org/10.1055/s-0029-1240902.
15. Wang G, Feng CC, Chu SJ, Zhang R, Lu YM, Zhu JS, Zhang J. Toosendanin inhibits growth and induces apoptosis in colorectal cancer cells through suppression of AKT/GSK-3β/β-catenin pathway. Int J Oncol. 2015;47:1767–74. https://doi.org/10.3892/ijo.2015.3157.
16. Kai W, Yating S, Lin M, Kaiyong Y, Baojin H, Wu Y, Fangzhou Y, Yan C. Natural product toosendanin reverses the resistance of human breast cancer cells to adriamycin as a novel PI3K inhibitor. Biochem Pharmacol. 2018;152:153–64. https://doi.org/10.1016/j.bcp.2018.03.022.
17. Wang X, Wang C, Wang Z. Determination of toosendanin in rat plasma by ultra-performance liquid chromatography-electrospray ionization-mass spectrometry and its application in a pharmacokinetic study. Biomed Chromatogr. 2013;27(2):222–7. https://doi.org/10.1002/bmc.2779.
18. Lu X, Ji C, Tong W, Lian X, Wu Y, Fan X, Gao Y. Integrated analysis of microRNA and mRNA expression profiles highlights the complex and dynamic behavior of toosendanin-induced liver injury in mice. Sci Rep. 2016;6(1):34225. https://doi.org/10.1038/srep34225.
19. Gupta J, Safdari HA, Hoque M. Nanoparticle mediated cancer immunotherapy. Semin Cancer Biol. 2021;69:307–24. https://doi.org/10.1016/j.semcancer.2020.03.015.
20. Yusuf A, Almotairy ARZ, Henidi H, Alshehri OY, Aldughaim MS. Nanoparticles as drug delivery systems: a review of the implication of nanoparticles' physicochemical properties on responses in biological systems. Polymers (Basel). 2023;15:1596. https://doi.org/10.3390/polym15071596.
21. Li H, Sun J, Zhu H, Wu H, Zhang H, Gu Z, Luo K. Recent advances in development of dendritic polymer-based nanomedicines for cancer diagnosis. WIREs Nanomed Nanobiotechnol. 2021;13:e1670. https://doi.org/10.1002/wnan.1670.
22. George A, Shah PA, Shrivastav PS. Natural biodegradable polymers based nano-formulations for drug delivery: a review. Int J Pharm. 2019;561:244–64. https://doi.org/10.1016/j.ijpharm.2019.03.011.
23. Rahmani F, Atabaki R, Behrouzi S, Mohamadpour F, Kamali H. The recent advancement in the PLGA-based thermo-sensitive hydrogel for smart drug delivery. Int J Pharm. 2023;631:122484. https://doi.org/10.1016/j.ijpharm.2022.122484.
24. Danhier F, Ansorena E, Silva JM, Coco R, Le Breton A, Preat V. PLGA-based nanoparticles: an overview of biomedical applications. J Control Release. 2012;161:505–22. https://doi.org/10.1016/j.jconrel.2012.01.043.
25. Luo L, Liang Y, Fu Y, Liang Z, Zheng J, Lan J, Shen F, Huang Z. Toosendanin induces hepatocyte damage by inhibiting autophagic flux via TFEB-mediated lysosomal dysfunction. Pharmaceuticals (Basel). 2022;15(12):1509. https://doi.org/10.3390/ph15121509.
26. Liang Y, Chen S, Han S, Luo L, Shen F, Huang Z. Toosendanin induced hepatotoxicity via triggering PERK-eIF2α-ATF4 medi ated ferroptosis. Toxicol Lett. 2023;377:51–61. https://doi.org/10.1016/j.toxlet.2023.02.006.
27. Sun M, Liu Q, Liang Q, Gao S, Zhuang K, Zhang Y, Zhang H, Liu K, She G, Xia Q. Toosendanin triggered hepatotoxicity in zebrafish via inflammation, au tophagy, and apoptosis pathways. Comp Biochem Physiol C Toxicol Pharmacol. 2021;250: 109171. https://doi.org/10.1016/j.cbpc.2021.109171.
28. Neophytou CM, Panagi M, Stylianopoulos T, Papageorgis P. The role of tumor microenvironment in cancer metastasis: molecular mec hanisms and therapeutic opportunities. Cancers (Basel). 2021;13(9):2053. https://doi.org/10.3390/cancers13092053.
29. Okada S, Vaeteewoottacharn K, Kariya R. Application of highly immunocompromised mice for the establishment of Patient-Derived Xenograft (PDX) Models. Cells. 2019;8(8):889. https://doi.org/10.3390/cells8080889. (Published 2019 Aug 13).
30. Iqbal M, Zafar N, Fessi H, Elaissari A. Double emulsion solvent evaporation techniques used for drug encapsulation. Int J Pharm. 2015;496:173–90. https://doi.org/10.1016/j.ijpharm.2015.10.057.
31. Bohrey S, Chourasiya V, Pandey A. Polymeric nanoparticles containing diazepam: preparation, optimization, characterization, in-vitro drug release and release kinetic study. Nano Converg. 2016;3(1):3. https://doi.org/10.1186/s40580-016-0061-2.
32. Longley DB, Harkin DP, Johnston PG. 5-fluorouracil: mechanisms of action and clinical strategies. Nat Rev Cancer. 2003;3:330–8. https://doi.org/10.1038/nrc1074.
33. Pakulska MM, Elliott Donaghue I, Obermeyer JM, et al. Encapsulation-free controlled release: Electrostatic adsorption eliminates the need for protein encapsulation in PLGA nanoparticles. Sci Adv. 2016;2:e1600519. https://doi.org/10.1126/sciadv.1600519.
34. Ma G. Microencapsulation of protein drugs for drug delivery: strategy, preparation, and applications. J Control Release. 2014;193:324–40. https://doi.org/10.1016/j.jconrel.2014.09.003.
35. Ndumiso M, Buchtová N, Husselmann L, et al. Comparative whole corona fingerprinting and protein adsorption thermodynamics of PLGA and PCL nanoparticles in human serum. Colloids Surf B Biointerfaces. 2020;188:110816. https://doi.org/10.1016/j.colsurfb.2020.110816.
36. Ferrari E, Pezzi ME, Cassi D, Pertinhez TA, Spisni A, Meleti M. Salivary cytokines as biomarkers for oral squamous cell carcinoma: a systematic review. Int J Mol Sci. 2021;22(13):6795. https://doi.org/10.3390/ijms22136795.
37. Zhang J, Yang F, Mei X, Yang R, Lu B, Wang Z, Ji L. Toosendanin and isotoosendanin suppress triple-negative breast cancer growth via inducing necrosis, apoptosis and autophagy. Chem Biol Interact. 2022;351:109739. https://doi.org/10.1016/j.cbi.2021.109739.
38. Wang H, Wen C, Chen S, Wang F, He L, Li W, Zhou Q, Yu WK, Huang L, Chen J, et al. Toosendanin-induced apoptosis in colorectal cancer cells is associated with the kappa-opioid receptor/beta-catenin signaling axis. Biochem Pharmacol. 2020;177: 114014. https://doi.org/10.1016/j.bcp.2020.114014.
39. Shao S, Li S, Liu C, Zhang W, Zhang Z, Zhu S, Feng Y, Pan Y. Toosendanin induces apoptosis of MKN-45 human gastric cancer cells partly through miR-23a-3p-mediated downregulation of BCL2. Mol Med Rep. 2020;22(3):1793–802. https://doi.org/10.3892/mmr.2020.11263.
40. Yang F, Li L, Yang R, Wei M, Sheng Y, Ji L. Identification of serum microRNAs as potential toxicological biomarkers for toosendanin-induced liver injury in mice. Phytomedicine. 2019;58:152867. https://doi.org/10.1016/j.phymed.2019.152867.
41. Zhang L, Song J, Kong L, Yuan T, Li W, Zhang W, Hou B, Lu Y, Du G. The strategies and techniques of drug discovery from natural products. Pharmacol Ther. 2020;216:107686. https://doi.org/10.1016/j.pharmthera.2020.107686.
42. Dreher MR, Liu W, Michelich CR, Dewhirst MW, Yuan F, Chilkoti A. Tumor vascular permeability, accumulation, and penetration of macromolecular drug carriers. J Natl Cancer Inst. 2006;98:335–44. https://doi.org/10.1093/jnci/djj070.
43. Kalyane D, Raval N, Maheshwari R, Tambe V, Kalia K, Tekade RK. Employment of enhanced permeability and retention effect (EPR): Nanoparticle-based precision tools for targeting of therapeutic and diagnostic agent in cancer. Mater Sci Eng C Mater Biol Appl. 2019;98:1252–76. https://doi.org/10.1016/j.msec.2019.01.066.
44. Yu H, Pardoll D, Jove R. STATs in cancer inflammation and immunity: a leading role for STAT3. Nat Rev Cancer. 2009;9:798–809. https://doi.org/10.1038/nrc2734.
45. Alzahrani AS. PI3K/Akt/mTOR inhibitors in cancer: at the bench and bedside. Semin Cancer Biol. 2019;59:125–32. https://doi.org/10.1016/j.semcancer.2019.07.009.
46. Jiang M, Li B. STAT3 and its targeting inhibitors in oral squamous cell carcinoma. Cells. 2022;11:3131. https://doi.org/10.3390/cells11193131.
47. Yang T, Xu R, Huo J, Wang B, Du X, Dai B, Zhu M, Zhan Y, Zhang D, Zhang Y. WWOX activation by toosendanin suppresses hepatocellular carcinoma metastasis through JAK2/Stat3 and Wnt/beta-catenin signaling. Cancer Lett. 2021;513:50–62. https://doi.org/10.1016/j.canlet.2021.05.010.
48. Zhang T, Li J, Yin F, Lin B, Wang Z, Xu J, Wang H, Zuo D, Wang G, Hua Y, et al. Toosendanin demonstrates promising antitumor efficacy

in osteosarcoma by targeting STAT3. Oncogene. 2017;36:6627–39. https://doi.org/10.1038/onc.2017.270.
49. Yu L, Wei J, Liu P. Attacking the PI3K/Akt/mTOR signaling pathway for targeted therapeutic treatment in human cancer. Semin Cancer Biol. 2022;85:69–94. https://doi.org/10.1016/j.semcancer.2021.06.019.
50. Zhang C, Gao H, Liu Z, Lai J, Zhan Z, Chen Y, Huang H. Mechanisms involved in the anti-tumor effects of Toosendanin in glioma cells. Cancer Cell Int. 2021;21:492. https://doi.org/10.1186/s12935-021-02186-2.

Publisher's Note